JOURNAL OF SPACECRAFT AND ROCKETS
Vol. 36, No. 2, March–April 1999

Global Aeroheating Wind-Tunnel Measurements Using Improved Two-Color Phosphor Thermography Method

N. Ronald Merski*
NASA Langley Research Center, Hampton, Virginia 23681

Detailed aeroheating information is critical to the successful design of a thermal protection system (TPS) for an aerospace vehicle. NASA Langley Research Center's (LaRC) phosphor thermography method is described. Development of theory is provided for a new weighted two-color relative-intensity fluorescence theory for quantitatively determining surface temperatures on hypersonic wind-tunnel models and an improved application of the one-dimensional conduction theory for use in determining global heating mappings. The phosphor methodology at LaRC is presented including descriptions of phosphor model fabrication, test facilities, and phosphor video acquisition systems. A discussion of the calibration procedures, data reduction, and data analysis is given. Estimates of the total uncertainties (with a 95% confidence level) associated with the phosphor technique are shown to be approximately 7–10% in LaRC's 31-Inch Mach 10 Tunnel and 8–10% in the 20-Inch Mach 6 Tunnel. A comparison with thin-film measurements using 5.08-cm-radius hemispheres shows the phosphor data to be within 7% of thin-film measurements and to agree even better with predictions via a LATCH computational fluid dynamics (CFD) solution. Good agreement between phosphor data and LAURA CFD computations on the forebody of a vertical takeoff/vertical lander configuration at four angles of attack is also shown. In addition, a comparison is given between Mach 6 phosphor data and laminar and turbulent solutions generated using the LAURA, GASP, and LATCH CFD codes on the X-34 configuration. The phosphor process outlined is believed to provide the aerothermodynamic community with a valuable capability for rapidly obtaining (three to four weeks) detailed heating information needed in TPS design.

Nomenclature

A = area of camera array element, m^2
a = effective aperture factor of camera optics, sr
b = vehicle wing span from wing tip to wing tip, m
C = heat transfer coefficient constant, $h(i_w/Tw)$
c = specific heat of model substrate, J/(kg-K)
D = driver constant, $i_{aw}(T_w/i_w) - T_{init}$
F = flux of light, W/m^2
h = heat transfer coefficient, kg/(m^2-s)
I = radiant intensity, W/(m^2-sr)
i = enthalpy, J/kg
j = fluorescence emission source term, W/(m^3-sr)
K = coating coefficient
k = thermal conductivity of model substrate, W/(m-K)
L = configuration length
M = Mach number
Pr = Prandtl number
Q = radiant power, W
$\dot{q}$ = heat transfer rate per unit area, W/m^2
r = recovery factor
T = temperature, K
t = time, s
x = axial location on configuration, m
y = spanwise location, m
z = distance into substrate, m
α = vehicle angle of attack
β = thermal product, $\sqrt{\rho ck}$, J/(m^2-K-s$^{1/2}$)
γ = ratio of specific heats
Δ = weighted logarithmic difference
η = ratio of fluorescence exponents, ν_R and ν_G
θ = temperature minus initial temperature, K
κ = thermal diffusivity, $k/\rho c$, m^2/s
Λ = variable from Laplace transform, $C\sqrt{t/\beta}$
ν = fluorescence exponent
ρ = density, kg/m^3
τ = window transmissivity
$\Phi(T)$ = temperature-dependent fluorescence factor
ω = phosphor absorption coefficient, 1/m

Subscripts

aw = adiabatic wall conditions
conv = convective
e = boundary-layer edge conditions
eff = effective
G = green component fluorescent light
init = initial conditions
lamp = uv lamp
R = red component fluorescent light
run = wind-tunnel run data reduction time
tot = total conditions
uv = ultraviolet portion of spectrum
w = conditions at the model surface
λ = region of electromagnetic spectrum
∞ = freestream

Introduction

A NUMBER of fast-paced U.S. hypersonic vehicle initiatives, such as X-33, X-34, and X-38, have occurred over the past few years. Programs such as these need aeroheating information to define the environment a vehicle will experience during flight and thereby design the vehicle's thermal protection system (TPS). The two-color relative-intensity phosphor thermography methodology described herein is a revolutionary approach to obtaining such aeroheating information experimentally. With the efficiency of the approach, vehicle designers can obtain detailed global, quantitative, parametric heating data within weeks after a request. Because of its usefulness, this method has played a significant role in recent vehicle programs. Recent applications of phosphor thermography include code comparison and crossflow transition studies on the McDonnell Douglas Delta Clipper vertical-takeoff/vertical-lander (VT/VL) configuration, a Shuttle Orbiter boundary-layer transition

Received April 3, 1998; revision received Dec. 23, 1998; accepted for publication Jan. 2, 1999.

*Aerospace Technologist, Aerothermodynamics Branch, Aero- and Gas-Dynamics Division, Research and Technology Group. Senior Member AIAA.

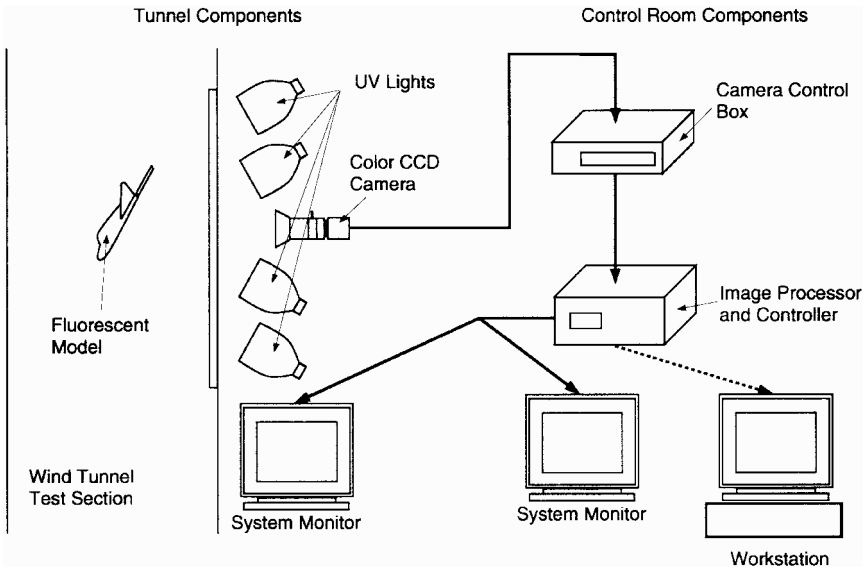

Fig. 1 Phosphor test setup.

roughness study,[1] parametric full configuration studies in support of Lockheed, Rockwell, and McDonnell Douglas X-33 phase 1 concepts, full configuration heating studies on the X-33 phase 2 (Refs. 2 and 3), X-34 (Ref. 4), and X-38 (Refs. 5–7) configurations, and finally, base heating for the Mars microprobe project.[8]

Early development of NASA Langley Research Center's phosphor thermography technique is described in Refs. 9–11. With this method, ceramic wind-tunnel models are fabricated and coated with phosphors that fluoresce in two regions of the visible spectrum when illuminated with ultraviolet light. One of the phosphors (ZnCdS:Ag, Ni) is a broadband thermographic phosphor fluorescing primarily in the green portion of the spectrum, and the other is a narrow-band rare earth (La_2O_2S:1%Eu), which has two green emission spikes and a red emission spike. The fluorescence intensity is dependent on the amount of incident ultraviolet light and the phosphor temperature. By acquiring fluorescence intensity images with a color video camera of an illuminated phosphor model exposed to flow in a wind tunnel (Fig. 1), surface temperature mappings can be obtained on the portions of the model that are in the field of view of the camera. The green and red camera outputs are utilized, and the resulting intensity images are entered into lookup tables created during the calibration of the system. With the present phosphors, a usable temperature range of 22–170°C is obtained. In addition, by the use of temperature mappings acquired at different times in a wind-tunnel run, heat transfer mappings are computed immediately following a run using the one-dimensional heat conduction equation.

This report presents an overview of the NASA Langley Research Center phosphor thermography method and highlights doctoral work that will be published in greater detail in the near future. First, a new weighted two-color relative-intensity phosphor thermography theory is introduced that enables a greater degree of accuracy in high-temperature global phosphor thermography measurements. In addition, an improved application of the one-dimensional heat conduction equation is presented that increases the accuracy of global heating data. Next, an overview of the phosphor thermography procedure, calibrations, and data reduction is given. Finally, comparisons of phosphor heating data to thin-film measurements and predictions from the LAURA, GASP, and LATCH CFD codes are presented.

Theory

Weighted Two-Color Relative-Intensity Fluorescence Theory

This section develops a weighted two-color relative-intensity theory for quantitatively determining temperature from measurement of fluorescent light emitted by a model's phosphor coating. In analyzing this problem, light from uv lamps illuminates the phosphor coating; the phosphor coating then emits visible light, which travels through a wind-tunnel window into the optics of a video camera and finally to a charge-coupled device (CCD) array. Ultimately, there are two primary unknown variables: the local surface temperature and the amount of local illumination of uv light on the model. A number of other factors (including model coating characteristics, facility window transmissivity, and optical response, among others) must be accounted for, however, or must be kept constant from the calibration process to the final data reduction.

The flux of uv light that excites the phosphor F_{uv} is equal to the flux of uv light from the lamps times a coating factor K_{uv}:

$$F_{uv} = K_{uv} F_{lamp} \tag{1}$$

The coating factor K_{uv} is dependent on the absorption rate of the phosphor coating, the coating thickness, surface reflectivity of the model surface, and incident angle of uv light on a model. A detailed understanding of the dependency of the coating factor on these variables can be obtained by using the radiative transfer equation.

The resulting emission response of the phosphors from the uv illumination is not necessarily linearly proportional to the amount of uv light incident on the model. Thus, unless the fluorescence characteristics are the same for two spectral bands or at two different temperatures, a straight ratio cannot be used to remove dependence on uv illumination as is often done for relative-intensity approaches. This situation is particularly true when phosphors are mixed that have different response characteristics to uv light. Not accounting for these fluorescence response characteristics can affect measurements on wind-tunnel models having local uv light illumination levels that significantly deviate from intensities used during calibration, particularly on configurations with large amounts of surface curvature. Reference 12 describes a number of possible curve fits for the nonlinear fluorescence response, the simplest of which is a power curve. A fluorescence emission source term j_λ (which is the intensity of fluorescent light per unit path length emitted by a phosphor illuminated with uv light), therefore, can be described by

$$j_\lambda = \Phi_\lambda(T) F_{uv}^{v_\lambda(T)} \tag{2}$$

All parameters in Eq. (2) are dependent on the region of the emission spectrum being modeled, and this band is denoted by the subscript λ.

The fluorescent intensity of light from the surface of the model can be expressed as j_λ times a coating function K_λ divided by an absorption coefficient ω_λ:

$$I_\lambda = j_\lambda K_\lambda / \omega_\lambda \tag{3}$$

Once the fluorescent phosphor light is emitted from the model surface, it passes through the tunnel window to the camera optics and reaches the camera CCD array. The radiant power of light that is incident on a CCD array element Q_λ can be expressed as

$$Q_\lambda = \tau_\lambda a I_\lambda A \tag{4}$$

Substitution of Eqs. (1–3) into Eq. (4) yields

$$Q_\lambda = [\tau_\lambda a_\lambda K_\lambda \Phi_\lambda(T) A/\omega_\lambda][K_{\text{uv}} F_{\text{lamp}}]^{\nu_\lambda(T)} \tag{5}$$

Equation (5) primarily depends on the amount of incident uv light on the model and the local temperature of the phosphor coating. To extract temperature from this equation, the dependence on uv light can be removed using a relative-intensity approach. By analyzing the fluorescence from the model within two different regions of the spectrum, two equations with two unknowns exist, and the uv light dependence can be removed. To do this, the natural logarithm is taken of Eq. (5) for two color components (in this case red and green):

$$\ell n(Q_R) = \ell n[\tau_R a K_R \Phi_R(T) A/\omega_R] + \nu_R(T)\, \ell n[K_{\text{uv}} F_{\text{lamp}}] \tag{6}$$

$$\ell n(Q_G) = \ell n[\tau_G a K_G \Phi_G(T) A/\omega_G] + \nu_G(T)\, \ell n[K_{\text{uv}} F_{\text{lamp}}] \tag{7}$$

At this point, a ratio of the fluorescence powers η is defined by

$$\eta = \nu_R/\nu_G \tag{8}$$

Multiplying Eq. (7) by Eq. (8) and subtracting the result from Eq. (6) causes the uv dependence to drop out, which yields the weighted two-color relative-intensity equation

$$\ell n(Q_R) - \eta(T)\, \ell n(Q_G) = \Delta(T) \tag{9}$$

where Δ is given by

$$\Delta(T) = \ell n[\tau_R a K_R \Phi_R(T) A/\omega_R] - \eta(T)\, \ell n[\tau_G a K_G \Phi_G(T) A/\omega_G] \tag{10}$$

To determine the temperature from Eq. (9), Δ and η must be calibrated as a function of temperature. Then given incident amounts of green and red light on the camera array (Q_G and Q_R, respectively), an iteration has to be performed with the Δ and η functions to back out the temperature.

Heat Transfer Theory

This section describes the theory used in the reduction of the phosphor thermography data to heat transfer mappings. In the reducing of the phosphor data, the phosphor coating is assumed to be infinitely thin, the convective heat transfer is assumed to be transmitted normally into the model surface, and the local surface radius of curvature is assumed to be large. The one-dimensional heat conduction equation can, therefore, be solved, which greatly simplifies the data reduction. The one-dimensional approach has its limitations, but for insulative ceramics such as fused silica and for short test times of less than a second, the approximation works well. In the development of the present heat transfer theory, the thermal properties of the fused silica will be assumed not to be dependent on temperature, and then a simple correction to account for this assumption will be described at the end of the section.

The governing one-dimensional heat conduction equation is given by

$$\rho c \frac{\partial \theta}{\partial t} = \frac{\partial}{\partial z}\left(k \frac{\partial \theta}{\partial z}\right) \tag{11}$$

With the assumption at this point that the thermal properties of the substrate material are constant, Eq. (11) becomes

$$\frac{\partial \theta}{\partial t} = \kappa \frac{\partial^2 \theta}{\partial z^2} \tag{12}$$

where $\kappa = k/\rho c$ is the thermal diffusivity of the substrate material.

To solve Eq. (12), one initial condition and two boundary conditions are required. For an initial condition, the temperature in a direction normal to the surface at a given location is assumed to be constant before the injection of the model in the wind tunnel:

$$\theta(z, 0) = 0 \tag{13}$$

For one of the boundary conditions, an infinite slab assumption is made whereby the temperature at some location into the model is always equal to the initial temperature:

$$\theta(\infty, t) = 0 \tag{14}$$

For the second boundary condition, the normal conduction into the wind-tunnel model is set equal to the convective surface heating:

$$-k \left.\frac{\partial \theta}{\partial z}\right|_{z=0} = \dot{q}_{\text{conv}} \tag{15}$$

where $\dot{q}_{\text{conv}}$ is the convective heat transfer rate per unit area.

The convective heating boundary condition is further assumed to experience a jump to a constant heat transfer coefficient during the injection of a model into a wind tunnel. Typically, for the development of similar data reduction approaches, the convective definition is temperature based; however, this assumption is strictly true only for a calorically perfect gas (gas with constant specific heats). In the case of the hypersonic facilities at NASA Langley Research Center, the reservoir temperature is past the limits of a calorically perfect gas, and an error can occur when using the temperature-based approach. Therefore, an enthalpy-based definition is used, where

$$\dot{q}_{\text{conv}} = h(i_{\text{aw}} - i_w) \tag{16}$$

To solve the conduction equation using Laplace transforms, the convective condition needs to be rewritten in terms of temperature. When a ratio of the surface enthalpy to surface temperature is pulled out, Eq. (16) can be rewritten as

$$\dot{q}_{\text{conv}} = h(i_w/T_w)[(T_w/i_w) i_{\text{aw}} - T_w] \tag{17}$$

For the temperature range over which the phosphor coating can detect, the air is calorically perfect, so that the ratio of the surface enthalpy to the surface temperature is nearly constant and the convection definition is now in a form that can be used with Laplace transforms.

With the substitution of Eq. (17) into Eq. (15), the surface boundary condition becomes

$$-k \left.\frac{\partial \theta}{\partial z}\right|_{z=0} = C(D - \theta_w) \tag{18}$$

where C and D are constants equal to $h(i_w/T_w)$ and $i_{\text{aw}}(T_w/i_w) - T_{\text{init}}$, respectively.

Equation (12) can now be solved with Laplace transforms using conditions given by Eqs. (13), (14), and (18). At the surface of the model, the solution is given by

$$\theta_w/D = 1 - e^{\Lambda^2} \text{erfc}\, \Lambda \tag{19}$$

where $\Lambda = C\sqrt{t/\beta}$. This equation is used for reducing the phosphor data.

Only an initial temperature and a temperature at some time into a tunnel run are required to solve Eq. (19). Thus, in a wind-tunnel run, an initial temperature image can be acquired before a run with no flow on the model, then a temperature image can be obtained during a run, and Eq. (19) can be solved at each pixel in the image. No temperature time history is needed. This is important with an imaging method because temperature histories of images would require a large amount of computer storage space.

The effect of using an enthalpy-based approach vs the conventional temperature-based approach is seen in Fig. 2. In the creation of Fig. 2, a conduction code was run with a constant heat transfer coefficient as the surface boundary condition. Heat transfer rates at a given time were next computed with both enthalpy-based and temperature-based approaches by solving Eq. (19) using the computer solution's surface temperature value and backing out $\dot{q}_{\text{conv}}$ from the appropriate convection definition, Eq. (16). Then the computed heat transfer rates were nondimensionalized with the heat transfer rate from the conduction solution. The resulting heat transfer ratios are plotted vs a temperature difference ratio, $(T_w - T_{\text{init}})/(T_{\text{tot}} - T_{\text{init}})$. From Fig. 2,

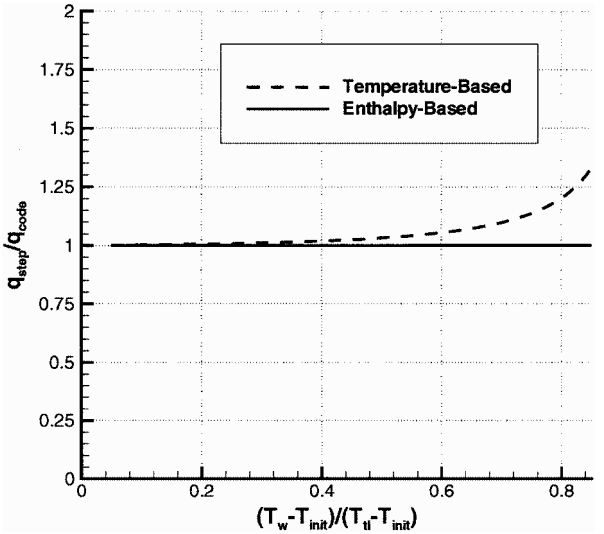

Fig. 2 Comparison of heat transfer rate computation between enthalpy-based and temperature-based methods.

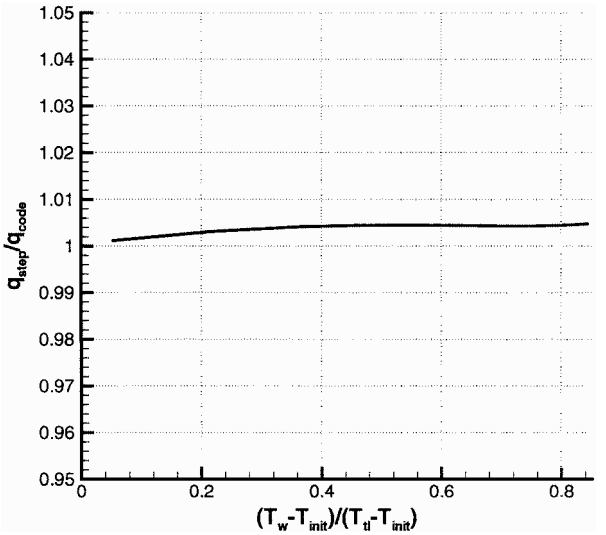

Fig. 3 Error of variable thermal properties approximation.

it can be seen that, as the wall temperature approaches the tunnel total temperature, the error with the temperature-based method begins to climb significantly, whereas the enthalpy-based method remains constant; thereby the need for an enthalpy-based approach is shown.

In reality, the time t in Eq. (19) does not start from the moment the model begins to heat. As the model travels through the test section wall boundary layer, the model does not experience a step in the heat transfer coefficient as was assumed in the heat transfer theory. Therefore, the injection process is modeled as a step in heating with the step in the heat transfer coefficient occurring at some time as the model passes through the boundary layer. The effective time at which the step occurs can be calibrated by acquiring data with a discrete gauge model. The heat transfer rate computed using a time-history-based method can then be put into Eq. (19) and a time backed out. Typical variations of the effective time on a model are between 1 and 2%. After performing a number of these calibrations, a simple approximation for determining the effective time has been observed:

$$t_{\text{eff}} = t_{\text{run}} - t_{\text{wall}} - (t_{\text{bl}} - t_{\text{wall}}) \times 0.5 \tag{20}$$

where t_{run} is the run time at which the data were acquired and t_{bl} is the time that the model reaches the edge of the tunnel boundary layer as determined from tunnel calibrations. This method of determining the effective time is currently the preferred approach. It effectively exchanges possible inconsistencies in the injection hydraulics with inconsistencies in the tunnel calibration profile.

The thermal product β in Eq. (19) is determined from a combination of thermal conductivity and thermal diffusivity measurements from the equation

$$\beta = k/\sqrt{\kappa} \tag{21}$$

For fused silica, thermal diffusivity and thermal conductivity samples have been tested, and the following curve fits dependent on temperature in degrees Kelvin have been computed from the resulting data:

$$\kappa = 9.212605264 \times 10^{-7} - 1.325181821 \times 10^{-9} T + 1.12667 \times 10^{-12} T^2 \tag{22}$$

$$k = 0.668170765 - 0.00068163 \times T \tag{23}$$

Up to this point, the heat transfer analysis has assumed that the thermal properties k, κ, and β are constant with respect to temperature, although this is not true. If room-temperature properties are assumed, as much as a 17% error can occur at the high end of the phosphor measurement range. For the phosphor thermography image data reduction, a relatively straightforward approach is proposed for correcting the variable properties effects. The thermal product at the initial room temperature β_{init} is averaged with the thermal product at the run temperature β_{run} to give an effective thermal product β_{eff} used for data reduction. Thus,

$$\beta_{\text{eff}} = \frac{\beta_{\text{init}} + \beta_{\text{run}}}{2} \tag{24}$$

To check Eq. (24), a one-dimensional infinite slab conduction code was run in a variable property mode for a range of heat transfer coefficients using the fused silica thermal properties curve fits [Eqs. (22) and (23)]. The output from the code was a series of temperatures through time, which were then reduced using Eq. (19). The results are plotted in Fig. 3. Here again, the ratio of reduced heat transfer rate to the heat transfer rate from the code, $q_{\text{step}}/q_{\text{code}}$, is plotted against the temperature difference ratio, $(T_w - T_{\text{init}})/(T_{\text{tot}} - T_{\text{init}})$. The heat transfer rates are seen to be within 0.5% for the full range of temperature difference ratios. This computational error is less than the errors associated with the thermal properties values themselves (which will be seen to be on the order of 6% in the error analysis section), and so Eq. (24) is believed to be sufficient for data reduction with fused silica substrates.

The last parameter needed in solving Eq. (19) is the adiabatic wall enthalpy i_{aw}, which is used to form the constant D. Improper determination of the adiabatic wall values is reported to lead to large uncertainties in computed heat transfer coefficients.[13,14] It is the contention of this work, however, that, inasmuch as the heat transfer coefficient is based on a definition [Eq. (16)], the uncertainties that are reported in the literature are not really uncertainties because a heat transfer coefficient calculated with an "incorrect" adiabatic wall enthalpy is just a heat transfer coefficient based on a different definition. The true uncertainty in the data reduction process lies in the uncertainties in the computed heat transfer rates on which inaccurate adiabatic wall conditions have a substantially lower effect. Figure 4 effectively illustrates this point with a plot of some typical heat transfer coefficient and heat transfer rate uncertainties for the same i_w/i_{aw} ratios. Based on this discussion, i_{aw} is typically set to the total enthalpy i_{tot} for phosphor data reduction.

In some cases at lower angles of attack or higher surface temperatures, however, uncertainties can become more significant. In such a case, the ratio of the adiabatic wall enthalpy to the total enthalpy can be found from the expression

$$\frac{i_{\text{aw}}}{i_{\text{tot}}} = \frac{1 + r[(\gamma - 1)/2]M_e^2}{1 + [(\gamma - 1)/2]M_e^2} \tag{25}$$

For laminar flows, r is assumed from viscous flow theory to be equal to $\sqrt{Pr}$, and for turbulent flow it is set equal to $Pr^{1/3}$. Typically, estimation of M_e using tangent-wedge or tangent-cone theory is

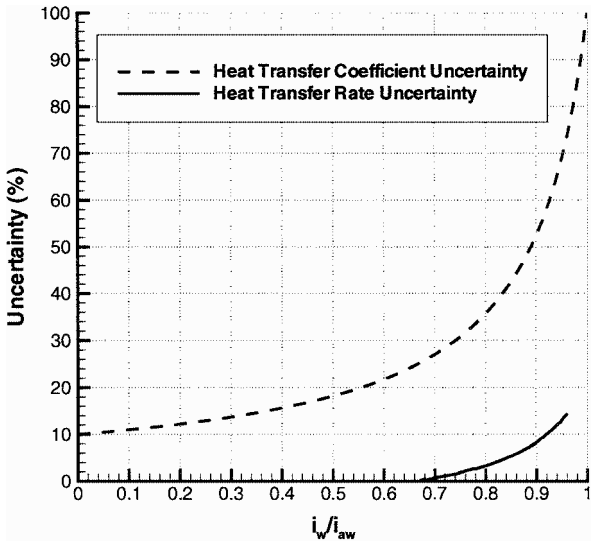

Fig. 4 Uncertainties in heat transfer computations with a 10% error in adiabatic wall enthalpy.

appropriate. Along the body, the adiabatic wall enthalpy decreases from the total enthalpy. For a global image where the local surface angle at a pixel may not be known, the strategy with laminar heating is to find the lowest adiabatic wall enthalpy on a configuration and then to average this result with the total enthalpy to obtain a global adiabatic wall enthalpy that splits the difference in possible errors in the image. In the case of turbulent heating where the flow trips back on the body, the adiabatic wall enthalpy is just selected as the adiabatic wall enthalpy on a wedge with an angle equal to the angle of attack of the vehicle.

Phosphor Thermography Method in NASA Langley Research Center Facilities

Model Fabrication

Fabrication of wind-tunnel models for phosphor testing is a critical component in the technique. To obtain accurate heat transfer data using the one-dimensional heat conduction equation, models need to be made of a material with a low thermal diffusivity and well-defined, uniform, isotropic thermal properties. Also, the models must be durable for repeated use in the wind tunnel, and they should be subject to minimal deformation when thermally cycled. To meet these requirements, NASA Langley Research Center has developed a unique, silica ceramic slip casting method.[15] Patterns for the models are typically made using a numerical cutting machine or with the stereolithography process. Using these patterns, investment molds are created. Ceramic slip is poured into the molds, and after the ceramic sets, the investment molds crumble off leaving ceramic shells. These shells are next fired in a kiln and potted with support hardware. The slip casting method allows for the casting of relatively fine details, as well as thin ceramic sections such as wings and fins. Model lengths are typically 0.2–0.3 m; however, models up to 0.75 m in length have been fabricated for testing at low angles of attack. In addition, the slip-casting method is a rapid process whereby, in two to three weeks, a full array of models can be fabricated, complete with various perturbations in a configuration, such as nose radius changes and control surface deflections.

Once the models are fabricated, they must be coated with phosphor crystals. Currently, the phosphors are suspended in a silica ceramic binder and applied with an airbrush. Final coating thicknesses have been measured to be approximately 25 μm. The coating method that has been developed produces robust coatings that do not require reapplication between runs; thereby the efficiency of the phosphor technique is significantly enhanced.

Facilities

NASA Langley Research Center's phosphor thermography method has been used in four of the facilities in NASA Langley's Aerothermodynamic Facilities Complex, which includes the 31-Inch Mach 10 Air, 20-Inch Mach 6 Air, 20-Inch Mach 6 CF_4, and 15-Inch Mach 6 High Temperature Tunnels. A detailed description of these facilities is given by Micol.[16] This section briefly describes the first two facilities, where the phosphor method has been primarily used to date.

The 31-Inch Mach 10 facility consists of high-pressure air storage rated to a maximum pressure of 30 MPa, a 12.5-MW electrical bundle heater that heats the air to approximately 1000 K, a settling chamber, three-dimensional contoured nozzle, test section, adjustable second minimum, aftercooler, vacuum spheres, and vacuum pumps. A 5-μm in-line filter, before the nozzle, removes particles from the airflow that can damage the ceramic phosphor models. The nozzle itself has a 2.7-cm square beryllium copper throat, and its exit height is 0.7874 m. The test section has a 0.75×0.45 m tempered-glass window for illuminating and viewing the phosphor models. Wind-tunnel models are protected from the flow as the tunnel comes to its operating condition by a door in the side wall of the test section. After the operating condition is reached, the model is injected to the tunnel centerline in approximately 0.55 s from the back side of the test section using a hydraulic injection system. Freestream Reynolds numbers obtained in this tunnel vary from 1.5×10^6 to 6.5×10^6/m.

The 20-Inch Mach 6 Tunnel has a two-dimensional contoured nozzle. The bottom and top walls of the nozzle are contoured and the side walls parallel. The test section size is 0.52×0.51 m and has tempered glass windows on the top and two sides. Models are mounted on an injection system in a housing below the test section. During a run, the models can be injected in less than 0.5 s. The tunnel has a range of operating reservoir pressures from 0.2 to 3.3 MPa and reservoir temperatures of up to 560 K. This corresponds to a freestream Reynolds number range of 1.5×10^6 to 25×10^6/m.

Acquisition Systems

Four phosphor thermography video acquisition systems have been constructed for use in NASA Langley Research Center's hypersonic facilities, two of which are currently operational and two of which will be brought online in the near future. The systems are composed of a color video camera with a zoom lens and a computer equipped with a digitizer. The camera has three CCD arrays, which obtain red, green, and blue component images (only red and green being used for phosphor thermography). Each array has 768 horizontal picture elements and 493 vertical picture elements. The signal from the color CCD arrays travels into a camera control box, which performs some analog signal processing. Processing features such as a gamma compensation circuit and a linear matrix circuit for obtaining lifelike color are disabled to help keep the response from the system linear.

Once the signal has been obtained and processed by the camera control box, it then proceeds to the acquisition computer, where the video frames are grabbed and digitized with an analog-to-digital converter (ADC). The ADC digitizes the signal to an eight-bit resolution, which corresponds to 256 discrete counts. Signal digitization can be modified by black and white level inputs to the ADC from the system software. Digital interlaced images can be obtained at the standard video rate of 30 frames per second with a spatial resolution of 640×480 pixels. The system can be put into a live-video mode with a pseudocolorcolor lookup table to set up the uv lighting on the models.

Tunnel Tests

To set up for a wind-tunnel run, the first task after mounting a model is to set up the uv lighting. The model is injected into the tunnel, and a monitor is set next to the test section, which displays a live pseudocolor image of the green component from the video camera. The lighting is set so that the fluorescence intensity from the model does not go over the scale limits of the phosphor system. This process is performed on the green component because this component decreases throughout a run and ultimately quenches out if a high enough temperature is reached. By keeping the green fluorescence intensity as high as possible without going overscale, the temperature range and resolution is optimized.

Once the lighting is set, the model is retracted and is ready for the tunnel run. The acquisition system is set to acquire images at

different times into the run. Because of possible conduction effects, earlier images provide data on high-heating, high-curvature portions of the model and later images provide data for low-heating, low-curvature portions of the model. After the acquisition system and tunnel are ready to run, the model is briefly injected into the tunnel test section, and a prerun image is obtained of the initial temperature distribution on the model. The model is retracted, and the tunnel is brought up to the desired reservoir pressure and temperature conditions. The model is then injected, the acquisition system is triggered, and the images are acquired at the preset times. Once the run has been completed, the images are saved and ported over to a UNIX-based workstation for data reduction and analysis.

Calibration

The phosphor thermography method has been developed to support work in a number of hypersonic facilities. In addition, as earlier stated, four acquisition systems have been made to support tests in these facilities. The ideal situation would be a total calibration process for one system, with one facility window and for one phosphor mix. However, with the number of systems involved, with the way acquisition systems can be shuttled between facilities, and with the batch-to-batch variations that can occur with the phosphors, the matrix of required calibrations can expand rapidly.

To reduce the number of calibrations that are required, a modular approach has been developed. Each system is calibrated individually for system response, each facility window is calibrated for transmissivity in the red and green portions of the spectrum, and the temperature/intensity response characteristics for each phosphor batch are calibrated separately. All of the calibrations are finally packaged together for any given combination via a lookup table creation program.

The first calibration required is to determine the response of the system to a given input of light Q for use in Eq. (9). To perform this, an acquisition system is pointed at an integrating sphere that is stepped through different intensity levels. Images are acquired at each level. From this analysis, a fourth-order fit is made for each color component of digital system response in counts vs light intensity. A sample red component calibration, along with the fit and a repeat run, is shown in Fig. 5.

In characterizing the facility window transmissivities, an integrating sphere is placed behind a window at an angle relative to the window. On the other side of the window, a camera is set up, and images are acquired of the integrating sphere port, with and without the window between the port and the camera. Red component and green component images are converted to light intensity mappings via the previous system response calibration, and the resulting mappings are averaged to yield window transmissivity factors in both the red and green portions of the spectrum.

The final calibration determines the fluorescence response characteristics of the phosphors at different temperatures. In performing this calibration, a thin 7.5-cm square plate coated with phosphors is placed into a computerized convection oven, which has a window on the front. The plate is illuminated with a uv lamp with a range of incident intensities from outside the oven. During a calibration, the plate is viewed with an acquisition system, and images are acquired at temperatures ranging from 22 to 170°C. The images at each temperature are analyzed, and $\log(Q_r)$–$\log(Q_g)$ lines are determined with slopes of $\eta(T)$ and y intercepts of $\Delta(T)$ as described by Eq. (9). A sample sweep of lines from a calibration is shown in Fig. 6. Once the slopes and intercepts have been determined, they are plotted and fit vs temperature as shown in Figs. 7 and 8.

Finally, lookup tables are created from the calibrations for use in the data reduction code IHEAT, which is discussed in the next section. When creating the lookup tables, variables are set corresponding to the results of the three calibrations, and a lookup table creation code iterates on each of the possible red and green acquisition readings. Ultimately a 256 × 256 array file containing temperatures is created. Given red- and green-component pixel outputs from the acquisition systems, the data reduction program can reference the lookup table to determine a temperature.

Data Reduction

Data reduction is performed in a UNIX-based, graphical user interface (GUI) program called IHEAT. This program efficiently handles the large amounts of image data associated with phosphor thermography calibrations, data reduction, and data analysis. When reducing the data, a setup file is first loaded into IHEAT. The setup

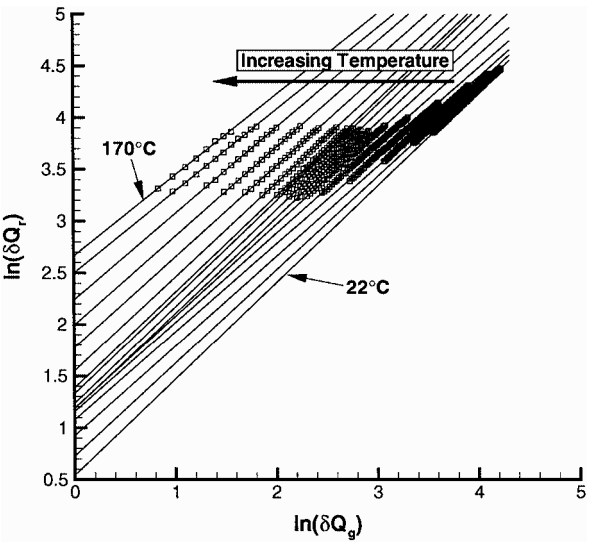

Fig. 6 Sweep of log–log lines.

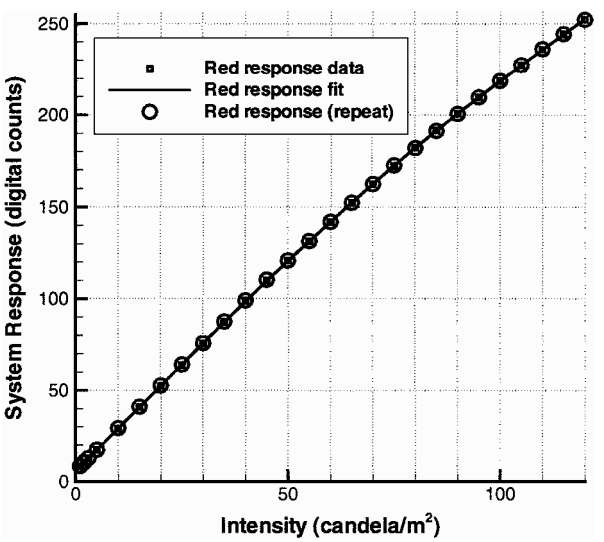

Fig. 5 Red component system calibration.

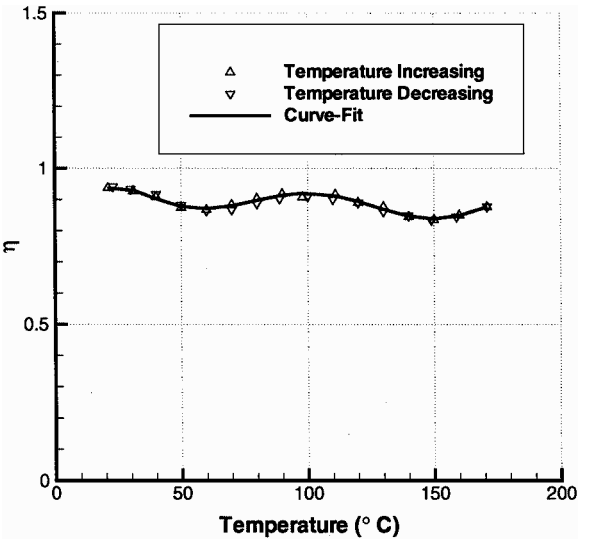

Fig. 7 Ratios of fluorescent exponents.

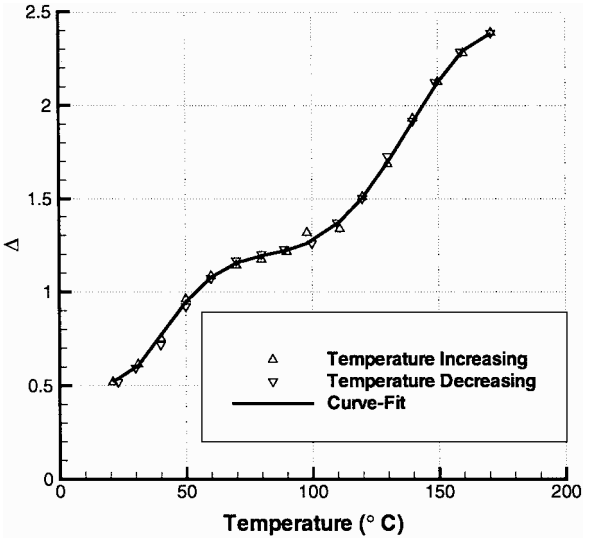

Fig. 8 Logarithmic differences.

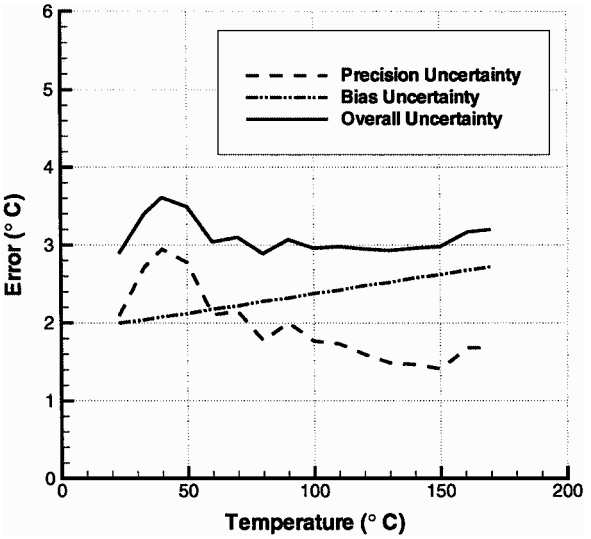

Fig. 9 Temperature errors.

file contains all of the specific information for the test setup, including phosphor system used, facility that the test is being performed in, and the phosphor mix that has been applied to the models. Once the setup file has been loaded, a file with the tunnel flow conditions for the run being analyzed is input. This file includes the tunnel total temperature, model angle of attack, and a predicted stagnation point heating value, which IHEAT uses to nondimensionalize the data. Next the position history of the model is input and analyzed to determine precisely the effective time at which the images are to be reduced. The prerun intensity images and run intensity images are input into IHEAT and immediately converted to temperature mappings.

Once the files have been loaded, the next step is to compute heat transfer coefficients. If an adiabatic wall enthalpy other than the tunnel total enthalpy is desired, an option exists that allows for the calculation of the adiabatic wall temperature on a wedge with a half-angle corresponding to the model angle of attack using Eq. (25). At this point, the global adiabatic wall temperature is known, along with the effective time and the model run and prerun temperatures. Equation (19) is then solved at every point that is in the field of view of the camera on the model to create heat transfer mappings.

After the heat transfer mappings have been computed, often line cuts from the image are desired. An automated approach exists in IHEAT to do this. Desired axial and longitudinal cut locations are entered into a window in IHEAT. Next, known fiducial mark locations in the image are clicked on and also input into IHEAT. Profile cuts are then extracted from the images at the desired locations, stretching the cuts according to the input fiducial mark locations. Once the cuts have been obtained, they are automatically saved for comparison with cuts from other runs.

Error Analysis

In analyzing the error for the phosphor thermography method, the AIAA standard for assessing wind-tunnel data uncertainty[17] was used, which in turn conforms with international guidelines and standards.[18] Although a number of different uncertainty sources exist for phosphor data, including those due to calibration, data acquisition, and processing; lack of fidelity in the models; knowledge of the tunnel test environment; three-dimensional conduction effects within the substrate; and registration of image pixel location to physical location on the model, this analysis reports errors associated only with the first two sources (calibration and data acquisition and processing), which are the most readily quantifiable. Errors are presented with bias limits, precision limits, and overall uncertainty (which is the square root of the sum of the uncertainties squared). All errors are reported with 95% confidence limits. The analysis describes the uncertainty associated with each variable in Eq. (19) (initial temperature, run temperature, adiabatic wall enthalpy, substrate thermal properties, and effective time) and then presents the combined uncertainty for all of the variables.

Temperature measurement uncertainties are plotted in Fig. 9. The bias error was determined from the uncertainty in the calibration oven temperature reading. The temperature distribution error through the oven test section was quoted to be 0.015°C and was considered negligible. The oven thermocouple uncertainty (furnished by the manufacturer) varied from 2 to 2.7°C. The precision error was found by putting the temperature calibration images (which theoretically are isothermal) into IHEAT and statistically looking at the temperature measured at each pixel element, calculating a standard deviation from the nominal temperature reading in the calibration, and multiplying by two for the 95% limits. From Fig. 9, the temperature error varies from 2.9 to 3.6°C. It is seen that the precision uncertainty dominates at the lower temperature, but then the bias uncertainty dominates the overall uncertainty at temperatures higher than 60°C. For the combined uncertainty analysis, the error in the initial temperature was assumed to be 2.9°C and the wall temperature error was assumed to be at the worst case of 3.6°C through the temperature range.

To compute the uncertainty in the adiabatic wall enthalpy, a worst-case situation was applied. The adiabatic wall enthalpy for a plate at 0-deg angle of attack was calculated and averaged with the tunnel total enthalpy. The difference between the averaged value and the tunnel total enthalpy was used as the error.

For the substrate thermal properties, the quoted instrumentation uncertainty was 3% for both the diffusivity and conductivity, and this was used as a bias uncertainty. A statistical analysis with a number of samples yielded precision uncertainties of 9.6 and 1.5% for diffusivity and conductivity, with corresponding overall uncertainties of 10 and 3.4%. The error due to choosing an average thermal product to account for thermal properties variations [Eq. (24)] was previously found to be 0.5% and was assumed to be insignificant. Although the diffusivity error seems large, the heat transfer rate is not ultimately as sensitive to it because a square root is taken of the diffusivity within the data reduction.

The effective time from Eq. (20) was found from thin-film calibration runs to have an uncertainty of 0.055 s. Thus, at 1 s, the error is 5.5%.

In determining a combined uncertainty, a standard approach is to use a first-order Taylor series expansion where sensitivities of variables within an equation are found by taking the partial derivative of the equation with respect to each variable within the equation. This approach is only valid, however, when a linear function is being analyzed. The function in Eq. (19) is not linear, and when a first-order Taylor series is used, artificially large errors arise due to the contribution of the adiabatic wall enthalpy. To properly compute the errors, higher-order terms in the Taylor series expansion must be used. This approach became impractical, and so a computer program was written where each of the variables in Eq. (19) was varied by its uncertainty, and the resulting heat transfer rate was compared with the heat transfer rate calculated with baseline values for the variables.

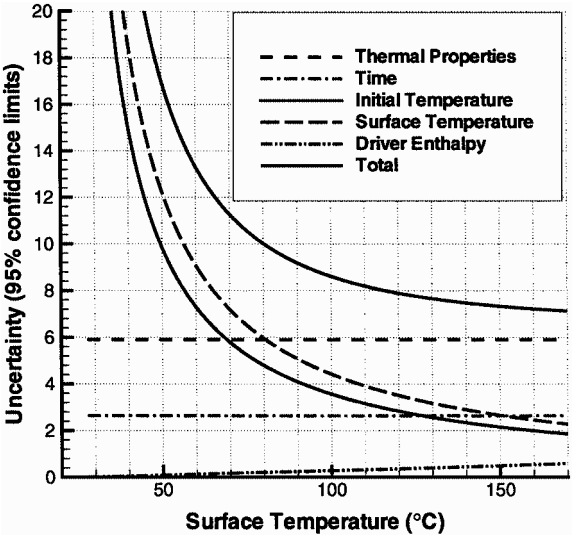

Fig. 10 Heat transfer rate errors in 31-Inch Mach 10 Tunnel.

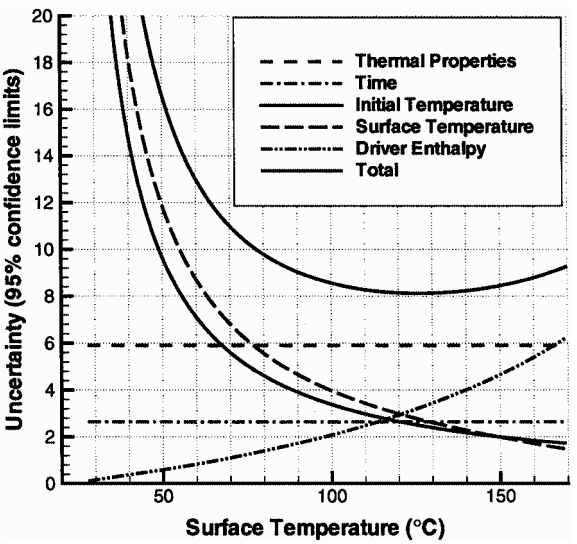

Fig. 11 Heat transfer rate errors in 20-Inch Mach 6 Tunnel.

Combined uncertainties in heat transfer rate for the phosphor data vs measured model surface temperature at 1 s into a run are plotted for the 31-Inch Mach 10 Tunnel and 20-Inch Mach 6 Tunnel in Figs. 10 and 11, respectively. From Figs. 10 and 11, it can be observed that the initial temperature and run temperature are the dominant uncertainties when lower surface temperatures are measured. Indeed, as the surface temperature approaches the initial temperature, the uncertainty climbs to infinity. This high error due to temperature is responsible for the large amount of scatter observed in phosphor heating data obtained from lower surface temperature readings. In most cases, however, the wall temperature measurements are higher, and the uncertainty due to thermal properties is the significant error source. In the case of the 20-Inch Mach 6 tunnel, at the higher end of the temperature range, the surface temperature to adiabatic wall temperature is much larger (due to the lower reservoir temperature of the tunnel), and the contribution of the error due to the adiabatic wall enthalpy is larger than in the case of the 31-Inch Mach 10 Tunnel. For the majority of the temperature range, the resulting total phosphor uncertainty varies between 7 and 10% in the 31-Inch Mach 10 tunnel and 8 and 10% in the 20-Inch Mach 6 tunnel.

Comparison to Thin-Film Hemisphere Measurements

A 5.08-cm-radius phosphor hemisphere model was fabricated and tested to compare with measurements on a 5.08-cm-radius hemisphere instrumented with thin-film resistance gauges. The phosphor hemisphere was made using the fabrication approach earlier

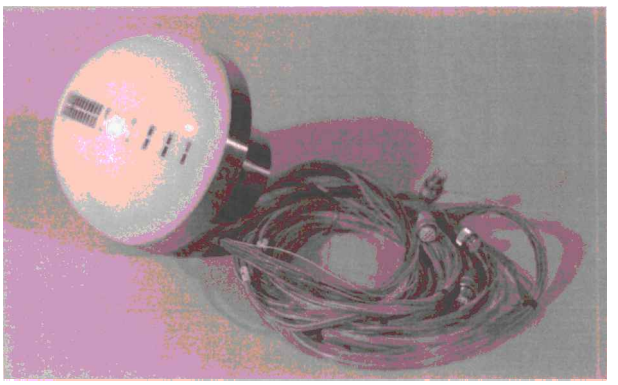

Fig. 12 Thin-film hemisphere.

described. A small fiducial mark was placed at the stagnation point to determine the stagnation point location in the run images. In the case of the thin-film hemisphere, the model (shown in Fig. 12) was made from MACOR® because the films could not be successfully applied to a fused silica substrate. Nine gauges were placed along an arc at 2.5-deg intervals from the stagnation point back to the 20-deg location. A gauge was placed at 25 deg and then from 30 to 70 deg in 10-deg increments. Four additional gauges were placed in 2.5-deg intervals back from the stagnation point on the other side of the model as a check on the symmetry of the measurements.

Both models were tested in the 31-Inch Mach 10 Tunnel at reservoir conditions of 5.0 MPa and 1000 K, corresponding to a freestream Reynolds number of 3.3×10^6/m. The phosphor data were reduced at a time of 1 s after the model had been exposed to the flow. The thin-film measurements were reduced with a data reduction code developed by Hollis,[19] which uses the Ref. 20 one-dimensional time history approach. All data were nondimensionalized using the Fay–Riddell[21] stagnation point heating values calculated using the stagnation point pressure gradient correlation developed by Inouye.[22]

Computational fluid dynamics (CFD) predictions were also made using the LATCH program for comparison with the wind-tunnel data. LATCH uses an axisymmetric analog for three-dimensional boundary layers with boundary-layer edge conditions from an inviscid flowfield solution.[23] LATCH computations for this comparison were performed, assuming equilibrium air properties, at wind-tunnel conditions, and were nondimensionalized in the same way as the wind-tunnel data.

A cut on the phosphor image was taken from the stagnation point to the aft end of the sphere. The phosphor data from the 80 to 90 deg locations were removed due to low uv illumination, which put the data out of the phosphor calibration range. Results are plotted along with the thin-film measurements and the LATCH predictions in Fig. 13. Two error bars, corresponding to the errors in the phosphor measurements, have been placed on the plot: One is near the front of the sphere with an uncertainty of $\pm 7.5\%$, and one is toward the back end of the sphere with an uncertainty of $\pm 15\%$. The phosphor data in the figure agree with the LATCH predictions, stagnation point theory, and thin-film results through the full 80 deg plotted in Fig. 13 to within the uncertainties of the phosphor technique, thereby providing a degree of confidence in the method. In the stagnation point region, the thin-film results are lower than the phosphor data, the computations, and the theory for reasons as yet to be determined. Low thermal properties used for the MACOR ceramic in the data reduction might be one possibility.

Computational Comparisons

Mach 10 8-Degree Sphere Cone Comparison

In support of the competitive first phase of the X-33 program, phosphor measurements were performed on a VT/VL configuration and compared with CFD predictions. The VT/VL model was 0.3048 m long, with a spherically blunted 8-deg cone forebody. The spherical nose was 2.54 cm in diameter. The conical forebody intersected a cylindrical aft section, which had cuts taken out of it at four circumferential locations 90 deg to each other. Flaps were located on each cut.

For this comparison, the LAURA CFD code was used for obtaining computational predictions. LAURA is an upwind-biased, point-implicit, three-dimensional, Navier–Stokes algorithm.[24] For the predictions presented here, the code was run in a laminar, perfect-gas, thin-layer Navier–Stokes mode.

The VT/VL model was tested in the 31-Inch Mach 10 Tunnel at 0-, 5.0-, 17.5-, and 25.0-deg angle of attack. The data were nondimensionalized with the stagnation point heating to a 2.54-cm-diam hemisphere, as calculated with the Fay–Riddell theory. CFD predictions were calculated using tunnel run conditions at each angle of attack. The CFD results at 17.5-deg angle of attack are compared with phosphor data in Fig. 14. In Fig. 14, good agreement on the conical forebody can be observed, although back on the flap (deflected at 20 deg), the phosphor data show substantially higher heating. The disagreement on the flap is believed to be due to the separated free-shear layer from the cone transitioning and reattaching on the flap, a flow situation that is challenging for CFD computations to predict.

Centerline cuts were also obtained at each angle of attack on the conical forebody only, and the results comparing the CFD predictions with the phosphor data are shown in Fig. 15. The results at the higher angles of attack show an initial drop in heating followed by a slight rise due to the occurrence of an overexpansion followed by a recompression in the nose region of the model. In general, at all angles of attack, there is very good agreement between the phosphor data and CFD predictions.

Mach 6 X-34 Comparison

CFD comparisons have also been made on an X-34 configuration (planform shown in Fig. 16) at Mach 6 conditions. For this study, 0.0183-scale phosphor models were fabricated and tested in the 20-Inch Mach 6 Tunnel at freestream Reynolds numbers varying from 1.9×10^6 to 25.6×10^6/m, as described in Ref. 4.

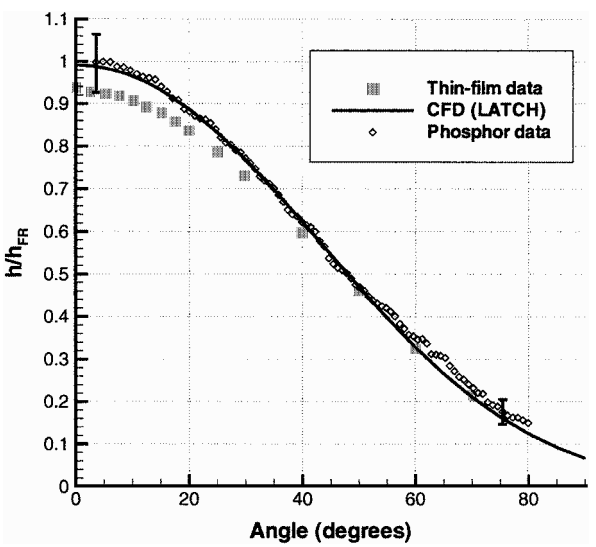

Fig. 13 Phosphor/thin-film hemisphere comparison.

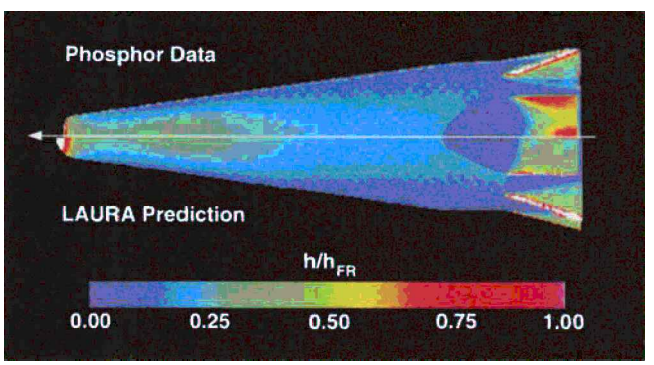

Fig. 14 VT/VL Mach 10 phosphor/LAURA comparison, α = 17.5 deg.

The CFD computations were performed using LAURA, LATCH, and GASP,[25] as described in Refs. 26, 27, and 4, respectively. The codes were run in laminar and turbulent perfect gas modes at tunnel conditions corresponding to a freestream Reynolds number of 25.6×10^6/m. The LAURA and the GASP calculations used the same grid, which was shock adapted from the LAURA code.

Comparisons between the laminar LAURA and GASP results and phosphor data are shown in Figs. 17 and 18. Turbulence results are shown in Figs. 19 and 20.

In the images, the phosphor data are seen to have a sharp jump in heating due to the onset of transition starting a third of the way back along the centerline. In comparing the phosphor data to the computational results, laminar predictions should be compared only with laminar phosphor data and turbulent predictions with turbulent data. The images show that the GASP predictions appear to run higher than the LAURA predictions in both the laminar and turbulent cases.

Line cuts were taken from the phosphor and CFD results along the centerline and at axial stations (shown in Fig. 16) of $x/L = 0.2$ and 0.79, where L is defined to be from the nose to the junction

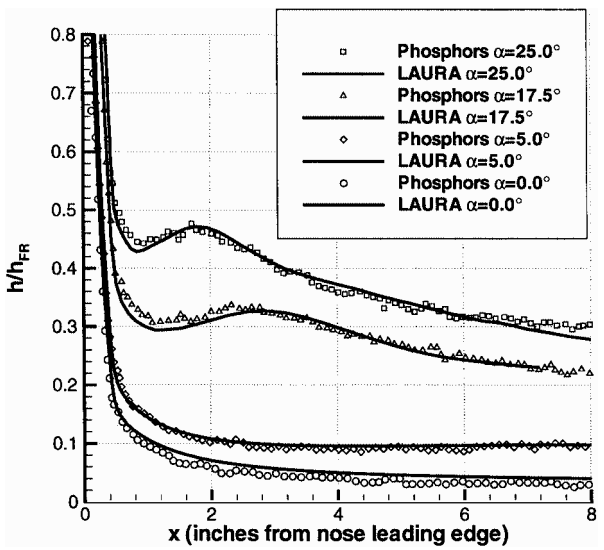

Fig. 15 VT/VL Mach 10 windward centerline heating comparison between phosphor data and LAURA computations.

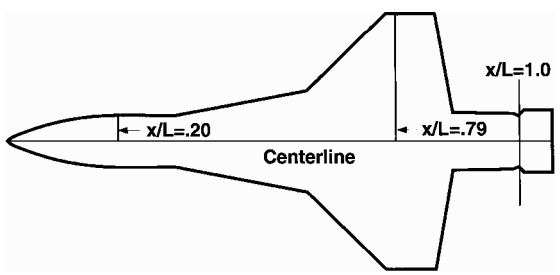

Fig. 16 X-34 planform with profile cut locations.

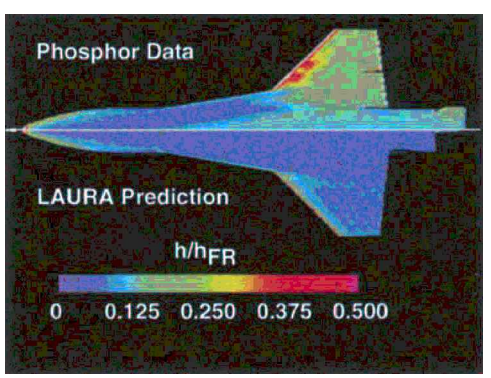

Fig. 17 Laminar phosphor/LAURA X-34 comparison, α = 15 deg.

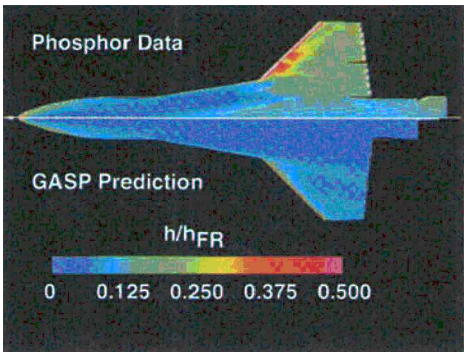

Fig. 18 Laminar phosphor/GASP X-34 comparison, α = 15 deg.

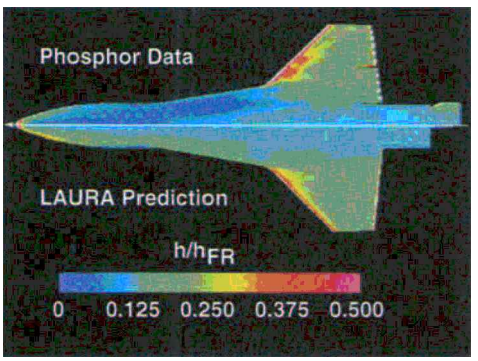

Fig. 19 Turbulent phosphor/LAURA X-34 comparison, α = 15 deg.

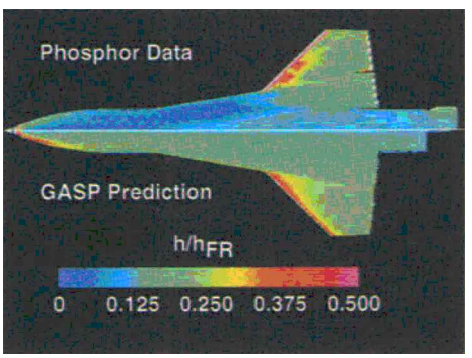

Fig. 20 Turbulent phosphor/GASP X-34 comparison, α = 15 deg.

between the flap and the fuselage. The centerline phosphor heating in Fig. 21 in the nose is laminar. A minimum is seen in the heating, and then the flow transitions to turbulence from an axial station of 0.25 to about 0.55. Agreement between the LAURA predictions and the phosphor data in both the laminar and turbulent regions is within experimental uncertainty. The GASP data tend to agree in the laminar region but are higher than the phosphor results in the turbulent region. The LATCH results split the difference between the LAURA and GASP results in the turbulent region but are higher than the phosphor data and LAURA and GASP predictions in the laminar region.

Figure 22 shows laminar comparisons at the 0.2 axial station with respect to $2y/b$, where y is the spanwise location and b is the total span from wing tip to wing tip. The LAURA predictions agree with the phosphor data to within the data uncertainty for most of the cut, whereas the GASP predictions tend to run a little higher than the phosphor data and the other predictions. The LATCH predictions start off higher than the phosphor data near the centerline and end up low outboard on the fuselage.

In the case of the 79% cut (Fig. 23), accurately predicting the heating is more difficult because of the presence of the bow shock/wing shock interaction on the wing. Along the cut from the centerline, the heating experiences a rise as the heating from the wing/fuselage junction is reached. This first rise is seen in the phosphor data, as

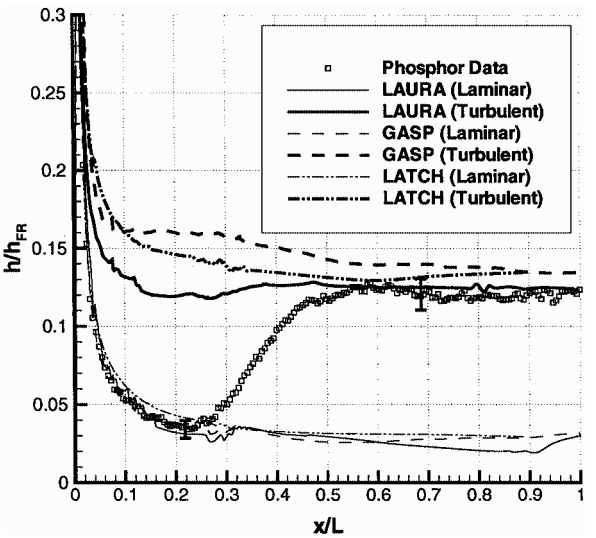

Fig. 21 Phosphor/CFD X-34 centerline comparison.

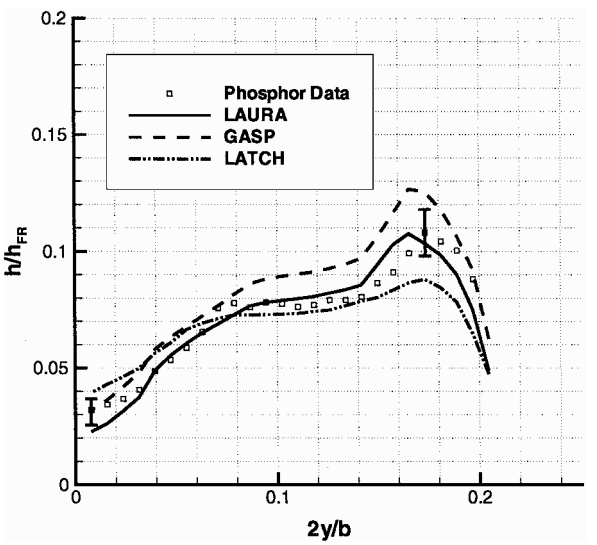

Fig. 22 Laminar phosphor/CFD X-34 comparison at x/L = 0.2.

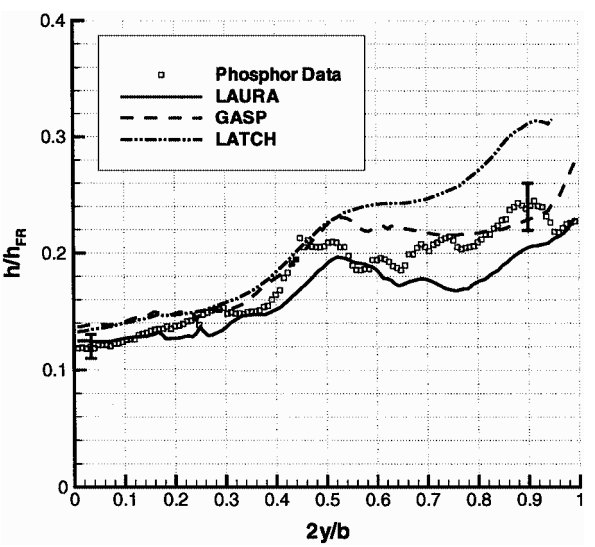

Fig. 23 Turbulent phosphor/CFD X-34 comparison at x/L = 0.79.

well as the computational predictions. As the bow shock interaction is reached (seen by the second and third humps in the phosphor data), however, the computations tend to smear out the heating levels. The LAURA and GASP predictions show a single slight rise in the heating but not to the same levels as the heating from the wing/fuselage junction, as is the case with the phosphor data. The LATCH code, however, misses the shock interaction completely.

Concluding Remarks

This paper has presented the basic process that is used at the NASA Langley Research Center in obtaining phosphor thermography data in hypersonic facilities. A new weighted relative-intensity fluorescence theory allows for the quantitative determination of surface temperature measurements on complex models having large amounts of surface curvature. Application of an enthalpy-based approach to solving the heat conduction equations, along with calibration of the effective starting time of a run and a simple approach for accounting for variable substrate thermal properties, improves the accuracy of global heat transfer computations. A user-friendly GUI data reduction code IHEAT allows for the rapid reduction and analysis of the large amount of image data associated with phosphor thermography. Coupled with this process is a rapid ceramic model casting technique. The result is a methodology that quickly provides a wealth of information critical to the design of a thermal protection system including effects of Reynolds number, Mach number, angle of attack, control surface deflection, and sideslip angle.

Acknowledgments

The following people are gratefully acknowledged for their contributions to this work: C. Riley for his LAURA vertical-takeoff/vertical-landing centerline solutions, S. Berry and T. Horvath for the X-34 phosphor data, and B. Wood and C. Glass for the 15-deg laminar and turbulent X-34 LAURA and GASP solutions, respectively.

References

[1]Berry, S. A., Bouslog, S. A., Brauckmann, G. J., and Caram, J. M., "Boundary Layer Transition Due to Isolated Roughness: Shuttle Results from the LaRC 20-Inch Mach 6 Tunnel," AIAA Paper 97-0273, Jan. 1997.

[2]Thompson, R., Hamilton, H., Berry, S., Horvath, T., and Nowak, R., "Hypersonic Boundary-Layer Transition for X-33 Phase II Vehicle," AIAA Paper 98-0867, Jan. 1998.

[3]Hamilton, H. H., Weilmuenster, K. J., Horvath, T. J., and Berry, S. A., "Computational/Experimental Aeroheating Predictions for X-33 Phase II Vehicle," AIAA Paper 98-0869, Jan. 1998.

[4]Berry, S. A., Horvath, T. J., DiFulvio, M., Glass, C. E., and Merski, N. R., "X-34 Experimental Aeroheating at Mach 6 and 10," *Journal of Spacecraft and Rockets*, Vol. 36, No. 2, 1999, pp. 171–178.

[5]Campbell, C. H., Caram, J. M., Berry, S. A., Horvath, T. J., and Merski, N. R., "An Overview of X-38 Hypersonic Aerothermodynamic Wind Tunnel Data and Comparison with Numerical Results," AIAA Paper 97-2475, June 1997.

[6]Berry, S. A., Horvath, T. J., and Williams, G. B., "Results of Aerothermodynamic and Boundary Layer Transition Testing of 0.0362-Scale X-38 (Rev 3.1) Vehicle in NASA Langley 20-Inch Mach 6 Tunnel," NASA TM-112857, Sept. 1997.

[7]Loomis, M. P., Venkatapathy, E., Papadopoulos, P., Davis, C. B., Campbell, C., Berry, S. A., and Horvath, T. J., "Aeroheating and Aerodynamic CFD Validation and Prediction for the X-38 Program," AIAA Paper 97-2478, June 1997.

[8]Mitcheltree, R., DiFulvio, M., Horvath, T., and Braun, R., "Aerothermal Heating Predictions for Mars Microprobe," AIAA Paper 98-0170, Jan. 1998.

[9]Buck, G. M., "An Imaging System for Quantitative Surface Temperature Mapping Using Two-Color Thermographic Phosphors," Instrument Society of America, ISA Paper 88-0772, May 1988.

[10]Buck, G. M., "Surface Temperature/Heat Transfer Measurement Using a Quantitative Phosphor Thermography System," AIAA Paper 91-0064, Jan. 1991.

[11]Merski, N. R., "A Relative-Intensity Two-Color Phosphor Thermography System," NASA TM-104123, Sept. 1991.

[12]Garlick, G., *Luminescent Materials*, Clarendon, Oxford, England, UK, 1949, pp. 1–6, 18–24.

[13]Stone, D. R., Harris, J. E., Throckmorton, D. A., and Helms, V. T., "Factors Affecting Phase-Change Paint Heat-Transfer Data Reduction with Emphasis on Wall Temperatures Approaching Adiabatic Conditions," AIAA Paper 72-1030, Jan. 1972.

[14]Nutt, K. W., "Thermographic Phosphor Technique," *Measurement Techniques for Hypersonic Flows*, Lecture Series 1990-05, von Kármán Inst. for Fluid Dynamics, Rhode Saint Genèse, Belgium, 1990, pp. 11–14.

[15]Buck, G. M., and Vasquez, P., "An Investment Ceramic Slip-Casting Technique for Net-Form, Precision, Detailed Casting of Ceramic Models," U.S. Patent 5,266,252, Nov. 1989.

[16]Micol, J. R., "Langley Aerothermodynamic Facilities Complex: Enhancements and Testing Capabilities," AIAA Paper 98-0147, Jan. 1998.

[17]*AIAA Standard: Assessment of Wind Tunnel Data Uncertainty*, AIAA Standard S-071-1995, AIAA, Washington, DC, 1995.

[18]*Guide to the Expression of Uncertainty in Measurement*, corrected ed., International Organization for Standardization, Geneva, Switzerland, 1995.

[19]Hollis, B. R., "User's Manual for the One-Dimensional Hypersonic Experimental Aero-Thermodynamic (1DHEAT) Data Reduction Code," NASA CR-4691, Aug. 1995.

[20]Kendall, D. N., Dixon, W. P., and Schulte, E. H., "Semiconductors Surface Thermocouples for Determining Heat-Transfer Rates," *IEEE Transactions on Aerospace and Electronic Systems*, Vol. 3, No. 4, 1967, pp. 596–603.

[21]Fay, J. A., and Riddell, F. R., "Theory of Stagnation Point Heat Transfer in Dissociated Air," *Journal of the Aeronautical Sciences*, Vol. 25, No. 2, 1958, pp. 73–85.

[22]Inouye, M., "Blunt Body Solutions for Spheres and Ellipsoids in Equilibrium Gas Mixtures," NASA TN-D-2780, May 1965.

[23]Hamilton, H. H., Greene, F. A., and DeJarnette, F. R., "An Approximate Method for Calculating Heating Rates on Three-Dimensional Vehicles," AIAA Paper 93-2881, July 1993.

[24]Gnoffo, P. A., "An Upwind-Biased, Point-Implicit Relaxation Algorithm for Viscous, Compressible Perfect-Gas Flows," NASA TR TP-2953, Feb. 1990.

[25]"GASP Version 3, The General Aerodynamic Simulation Program, Computational Flow Analysis Software for the Scientist and Engineer, User's Manual," AeroSoft, Inc., Blacksburg, VA, 1996.

[26]Kleb, W. L., Wood, W. A., Gnoffo, P. A., and Alter, S. J., "Computational Aeroheating Predictions for X-34," *Journal of Spacecraft and Rockets*, Vol. 36, No. 2, 1999, pp. 179–188.

[27]Riley, C. J., Kleb, W. L., and Alter, S. J., "Aeroheating Predictions for X-34 Using an Inviscid Boundary-Layer Method," *Journal of Spacecraft and Rockets*, Vol. 36, No. 2, 1999, pp. 206–215.

I. E. Vas
Associate Editor

Color reproductions courtesy of NASA Langley Research Center